ADVANCED FUNCTIONAL MATERIALS
www.afm-journal.de

Nafion Matrix and Ionic Domain Tuning for High-Performance Composite Proton Exchange Membranes

Keenan Smith, Fabrizia Foglia, Adam J. Clancy, Dan J. L. Brett, and Thomas S. Miller**

Although proton exchange membranes (PEMs) are widely deployed in an array of commercial applications, limitations linked to their proton conductivity, water retention, and gas permeability still limit ultimate device performance. While ex situ studies have shown additives can enhance membrane stability and mass transport, to date few have demonstrated that these performance enhancements are maintained when tested in commercially relevant electrochemical technologies, such as fuel cells or electrolyzers. Herein, a new multifunctional additive, 2D poly(triazine imide) (PTI), is demonstrated for composite PEMs, which is shown to boost proton conductivity by 37% under optimal high relative humidity (RH) conditions and 67% at low RHs. PTI also enables major improvements (over 55%) in both current and power densities in industrially relevant PEM fuel cells (PEMFCs). Most importantly, in situ and ex situ characterization suggests that the enhanced performance is due to polymer aggregate-PTI clusters that form with increasing 2D character and improved long-range connectivity, while acid-base interactions with pyridinic nitrogen facilitate the critical proton hopping mechanism at all RHs. Hence, this work offers both a new membrane concept with proven benefits for important electrochemical technologies, as well as design principles for future optimization of proton transport and water management within PEMs.

1. Introduction

Proton exchange membranes (PEMs) are essential components of many emerging technologies, from fuel cells (FCs),[1] water electrolyzers (WEs),[2] and redox flow batteries,[3] to the electrochemical conversion of feedstocks, such as CO_2 and N_2.[4] Use of FCs and WEs to enable the use of hydrogen as a sustainable energy vector has become internationally recognized as an essential element of carbon neutral strategies. By enhancing the proton conductivity, water retention, and lifetime of PEMs while minimizing gas permeability, device efficiency can be increased, permitting the use of these devices in emerging applications, such as long-haul transport and aviation. High proton conductivity and good mechanochemical stability have positioned perfluorinated sulfonic acid (PFSA) polymers, such as Nafion, as the commercial standard PEM for the past half century.[5] Central to their superior performance is a complex semicrystalline polymer matrix that forms ion-conducting domains due to phase separation of hydrophobic polytetrafluoroethylene backbones and hydrophilic sulfonic acid terminated fluorinated ether side chains. Hydration induced water uptake (WU) and swelling above the percolation threshold forms contiguous proton conducting channels, allowing fast proton transport via a combination of Grotthuss hopping and vehicular diffusion.[6] This hydration-dependent conductivity necessitates careful water management to mitigate issues such as cell hydration heterogeneity due to electro-osmotic drag and water production at the cathode. Hybridization with complementary nanoparticle, nanotube, and nanosheet fillers has been used to enhance water management within PEMs and because of the high surface area interface between nanoparticle and polymer, significant improvements have been achieved with as little as 0.25 wt% additive, highlighting nanoparticle additives as a cheap and facile approach.[7–9]

Nafion ionic domains, constructed by ionic multiplets, are understood to assemble with 2D character.[10,11] Primary aggregate polymer fibrils (≈6 × 80 nm) are believed to phase separate with "lamellar,"[12] "sandwich-like,"[13] and "ribbon-like,"[14,15] ionic unit structures, and assemble into secondary aggregates of 50–100 nm bundles.[16] Lamellar ionic domains thus lend themselves to synergistic interactions with 2D additives such as graphene oxide (GO). As GO and sulfonated GO are hygroscopic and have proton hopping sites, high thermal stability, and a high surface area they have been shown to improve conductivity and gas crossover resistance.[17,18,20] However, graphene

K. Smith, D. J. L. Brett, T. S. Miller
Electrochemical Innovation Lab
Department of Chemical Engineering
University College London
London WC1E 7JE, UK
E-mail: d.brett@ucl.ac.uk; t.miller@ucl.ac.uk

K. Smith, F. Foglia, A. J. Clancy
Department of Chemistry
Christopher Ingold Laboratory
University College London
London WC1H 0AJ, UK

The ORCID identification number(s) for the author(s) of this article can be found under https://doi.org/10.1002/adfm.202304061

DOI: 10.1002/adfm.202304061

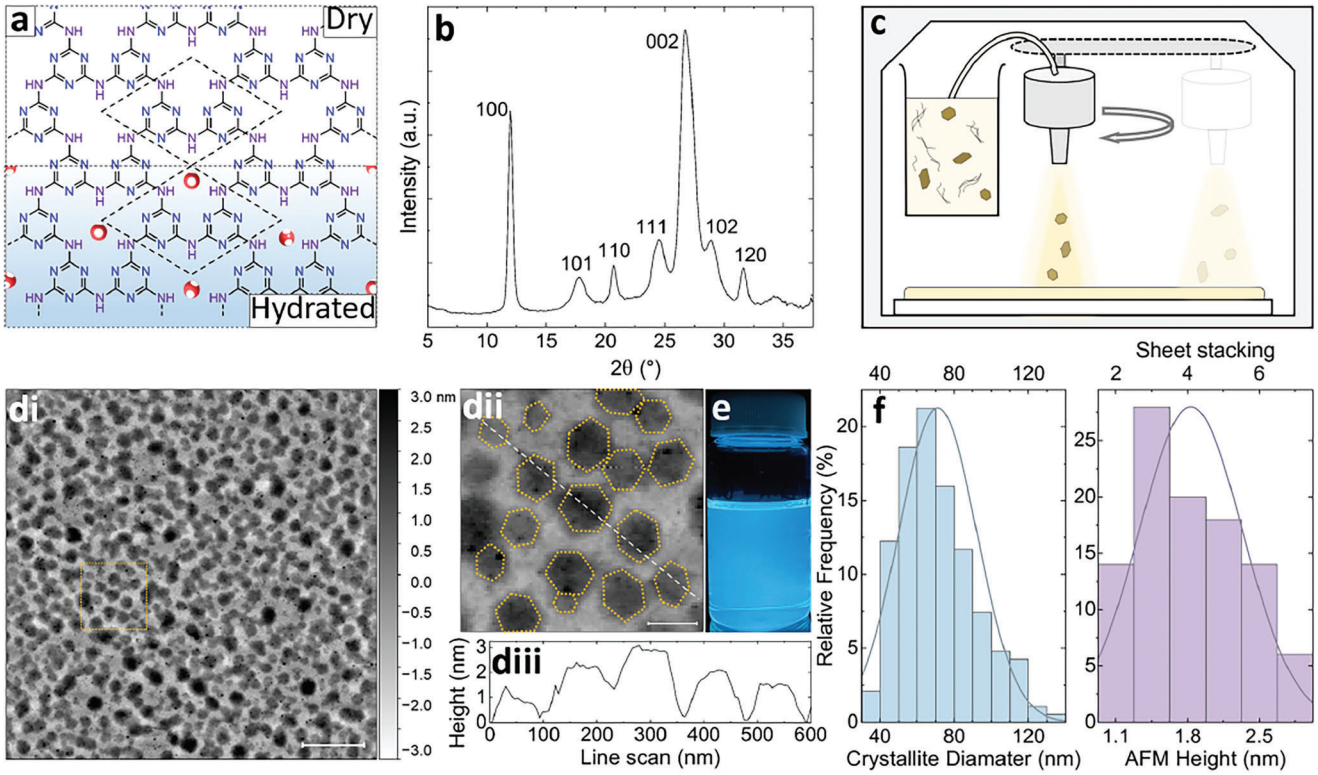

Figure 1. PTI characterization and fabrication protocol. a) Crystallographic structure of PTI with unit cell highlighted in both dry and hydrated environment, representing spontaneous water intercalation to $C_{12}N_{12}H_3$ voids at atmospheric humidity (red ball: oxygen atom, white ball: hydrogen atom). b) XRD of bulk PTI powder before exfoliation. c) Schematic of USP setup used to obtain PEM film from Nafion–PTI/DMF dispersion. di) AFM topography image of PTI deposited from a DMF based solution onto mica substrate (scale bar = 500 nm) ii) magnified view of the region highlighted in di, with particle shape highlighted (scale bar = 100 nm), and iii) height profile of five particles . e) Photograph of PTI/DMF solution under <365 nm UV illumination. f) Histograms showing crystallite diameter and thickness/sheet stacking from AFM measurements.

derivatives are thermally and electrochemically reduceable, resulting in poor long-term performance as a result of inert and electronically conducting particles within the PEM. Addition of electrochemically inert graphitic carbon nitrides (gCN) has been demonstrated to improve PFSA performance, reportedly due to a large surface area of NH functionalities complementing the hydrogen-bonding network and forming acid–base pairs, while its high surface area creates more tortuous paths and decreases fuel crossover.[19] However, to date only "polymeric/amorphous" gCN sheets with micrometer dimensions have been used, which have poor compatibility with the nanometer scale phases within PFSAs. Optimal improvements thus require fillers with favorable chemical properties and suitable size for appropriate structural tuning, such as the ≈5 nm hydrophilic quantum dots that Qiao et al[21] hypothesizeto locate within Nafion hydrophilic domains. However, hydrophilic additives that situate within the hydrophilic domains are at risk of leaching from the membrane over extended operation. In addition, steric impediment of side chain mobility, which facilitates dynamics of protons and water, and occupation of hydrated volume within the domain, raise concerns for the use of <10 nmadditives.[22]

2D poly(triazine imide) (PTI)-structured graphitic carbon nitride sheets, with diameters of 30–140 nm, have commensurate dimensions to those of Nafion main chains as well as primary and secondary aggregates, facilitating optimal integration and matrix tuning. **Figure 1**a shows the repeating $C_{12}N_{12}H_3$ structural voids with triazine/pyridinic and bridging N–H groups found in intercalant free PTI, and water intercalation sites that spontaneously fill in ambient RH. These hydrophilic groups provide a source of additional (de-)protonation sites and promote intralayer water transport,[23,24] collectively capable of facilitating hydrated proton transport.[25] The macroscopic properties of the membrane not only depend on the size, shape, and functionalityof the dispersed particles, but also on their amount and orientation .[26] Scalable ultrasonic spray printing (USP) was used to prepare composite membranes with few-layer PTI nanosheets homogeneously dispersed into the Nafion framework, affording the greatest performance gain from additive–polymer interactions without exceeding the polymer matrix threshold limit.[27] The composite PEMs achieved significant improvements over commercially available Nafion, which were retained during and after accelerated stress testing (AST) showing the (electro-)chemical stability of PTI.[28]

2. Results

2.1. PTI Synthesis and Composite Fabrication

Bulk PTI·H_2O powder was prepared via molten salt synthesis of PTI·LiCl, and subsequent continuous Soxhlet extraction in deionized (DI) water to remove Li^+ and Cl^- ions. X-ray diffraction (XRD) is shown in Figure 1b, indicating a gallery height of 3.29 Å (002 peak).[29] Spontaneous dissolution in

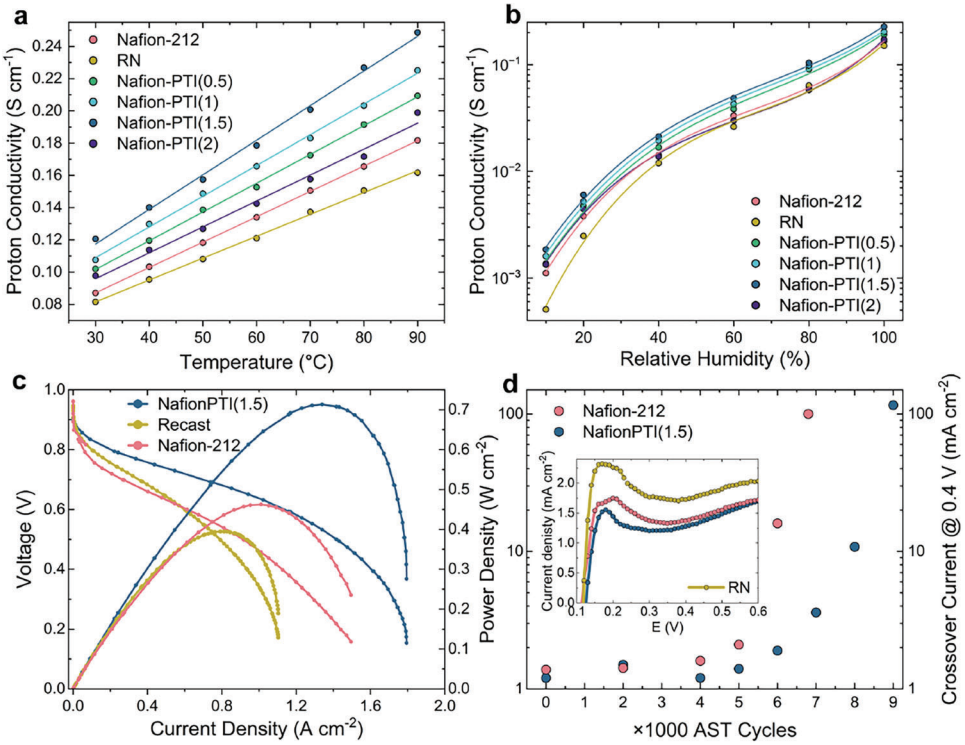

Figure 2. Electrochemical performance. Proton conductivity versus a) temperature at 100% RH (with linear fit) and b) RH at 80 °C (with polynomial fit to guide the reader). c) Single-cell FC testing operated at 80 °C and 100% RH showing polarization curve and power density plot with H_2/air (stoichiometric control of 1.5:3). d) Crossover current density from LSV at 0.4 V obtained during mechanochemical AST, with inset of beginning of life LSV conducted with H_2/N_2 0.2 L min^{-1}.

N,N-dimethylformamide (DMF) yielded a clear, yellow solution of PTI/DMF saturated after 10 days, which fluoresced under UV-light (<365 nm) illumination (Figure 1e).[30] Atomic force microscopy (AFM) of deposited aliquots (Figure 1d), along withstatistical analysis of crystallite diameters and heights, confirmed the solution contained PTI sheets with lateral dimensions of 30–140 nm (70 nm average) and primarily quadruple layer stacking (2–7 sheet stacks) (Figure 1f). Compared to other exfoliated 2D materials, PTI exhibits a narrow size distribution which provides an attractive filler material with a consistent effect, and particle size can be further tuned by employing growth cycles or specific growth times.[31]

The PFSA precursor was prepared following the method reported by Moore and Martin,[32] due to the superior physicochemical properties found and the compatibility of "solution-processed" Nafion with DMF. The PFSA powder was dispersed in a specific volume of PTI/DMF to achieve the desired mass fraction of PTI in the cast membrane (0.5–2 wt%) and deposited using USP on a flat glass substrate before annealing to give a membrane designated NafionPTI(*X*) where *X* = wt% of PTI (Figure 1c). A control membrane, recast Nafion "RN", was prepared using the same approach with pure DMF. Highly uniform membrane dimensions, with thicknesses accurate to 1 µm, were obtained using USP. This provides a scalable option for bespoke composite formulations to be used in advanced membrane electrode assembly (MEA) approaches, such as direct membrane deposition or multilayering.[33]

2.2. Electrochemical Performance

USP deposition produced films composed of an amalgamation of ≈10–50 µm spherical droplets observed on the surface but retained a homogeneous composition within the film interior, as seen in Figure S1 (Supporting Information). The macroscopic morphology had no detrimental effect on PEM performance with RN having a conductivity commensurate with commercial Nafion-212 membranes (**Figure 2**a). The slightly lower conductivity, commonly observed from recasting procedures, could be overcome by further optimization of the recasting and annealing process employed (i.e., temperature and duration). Incorporation of greater PTI quantities into the host matrix was found to provide corresponding enhancement to proton conductivity with a maximum achieved in NafionPTI(1.5), showing ≈50% greater conductivities compared to RN at all temperatures and a maximum of 0.248 ± 0.022 S cm^{-1} at 100% relative humidity (RH) and 90 °C (Figure 2a). Exceeding the apparent threshold limit had a deleterious outcome, with a reduced proton conductivity seen in NafionPTI(2), which could be from PTI-induced tortuosity, surplus PTI interactions slowing proton hopping, or restacking of PTI sheets. The effect of excess PTI was highlighted when fabricating the composites using the solvent casting method (SCM) (Figure S2, Supporting Information), where minor PTI induced improvements were observed, and a maximum conductivity was achieved at 1 wt% PTI before reductions for 1.5 and 2 wt%. Slow solvent evaporation duting the SCM permitted a heterogeneous nanofiller concentration profile to form through the PEM

thickness, and extended casting time allowed deleterious PTI agglomeration and restacking. USP appears to circumvent both of these issues with greater conductivity enhancement for each composition and addition of 0.5 wt% more PTI before the threshold limit was exceeded.[34] USP fabrication thus affords the greatest performance gain from additive–polymer interactions.

As seen in Figure 2a, conductivity continued to rise as temperature reached 80 and 90 °C in NafionPTI(1.5) and NafionPTI(2), where plateaus are commonly observed for Nafion due to reduced water content. Hygroscopic PTI has the capability to increase water retention at higher temperatures, potentially helping retainin the proton transport media. Alternatively, a new conduction mechanism could become activated at high temperatures, such as the temperature-dependent water transport within PTI voids.[24] Hydration is essential for the conduction mechanism within Nafion, seen for RN in Figure 2b, where a steep drop is observed towards the mid-RH plateau, as "free water" is lost below the percolation threshold, before another sharp drop is seen as proton hydration shells are lost at low RH. PTI buffered the initial steep conductivity loss with NafionPTI(1.5) having an 86% greater conductivity at 60% RH. A greater proportion of hydrated connected networks were retained suggesting an altered morphological arrangement with reduced tortuosity. At low RH, PTI supports conductivity, with NafionPTI(1.5) having a 144% greater conductivity at 20% RH, suggesting that PTI provides an additional source of hydration or proton coordination. NafionPTI(2) appeared to have negligible effect at intermediate RH, but enhanced conductivity at low RH. This difference provides some insight into the cause of the matrix threshold, where excess PTI still provides a beneficial increase in retained water at low RH but induces less efficient matrix tuning and greater tortuosity for long-range conduction at intermediate and high RH. While these conductivities are not suitable for nonhumidified or high-temperature applications, they are well placed to manage and moderate temperature and hydration heterogeneities within traditional low-temperature devices which are already commercialized.

H_2/air fuel cells (5 cm^2) were assembled using Nafion-212, RN, and NafionPTI(1.5) and achieved open-circuit voltages (OCVs) of 0.96, 0.95, and 0.94 V, respectively, validating MEA assembly for all samples. Gas crossover, due to the fuel concentration gradient across the membrane, reduces efficiency due to parasitic hydrogen consumption and mixed potentials on the cathode electrode. Beginning of life (BoL) H_2 crossover of 1.24 mA cm^{-2} for NafionPTI(1.5), taken at 0.4 V from the linear sweep voltammetry (LSV) plots in the inset of Figure 2d, which was 11% and 60% lower than Nafion-212 and RN at 1.38 and 1.99 mA cm^{-2}, respectively. Under optimal conditions of 80 °C and 100% RH, NafionPTI(1.5) achieved a maximum power density of 0.714 W cm^{-2}, compared to 0.462 W cm^{-2} for Nafion-212, while current density increased from 0.613 to 1.14 A cm^{-2} at 0.6 V (Figure 2c). Similar improvements in current and power density were observed when operating the FC at reduced RHs of 25% and 50%, due to the retention of hydrated ionic domains that support proton conduction at low RH (Figure S5, Supporting Information). Collectively, greater proton conduction and hydration management resulted in reduced electrolyte resistance and accelerated cathodic reactions, which combined with reduced gas crossover, delivered superior cell performance.

MEAs are subjected to considerable compressive forces during normal FC operation and, with additional high temperature and humidity variation, polymer deformation and creep can lead to pinholes and cell failure. PEM degradation is also compounded by chemical attack over extended fuel cell operation with radical attack initiated from H_2O_2 generated due to gas crossover.[35] PEMs thus require sufficient mechanical strength and chemical durability for long lifetime operation. These effects were studied using a reported AST protocol for mechanochemical stress, characterized by hydrogen crossover every 1000 cycles. Figure 2d shows crossover current measured during the AST for NafionPTI(1.5) and Nafion-212, which exceeded 8000 and 6000 cycles, respectively, before crossover exceeded 15 mA cm^{-2}. To this point, both exhibited continual minor drop in OCV, whereas at 6800 cycles, Nafion-212 displayed an onset of a large OCV loss of 29.2% compared to BoL with concomitant major crossover, characteristic of pinhole formation. In contrast, NafionPTI(1.5) exhibited half the OCV loss of only 13.3% after 7000 cycles. PTI mitigated effects of dimensional change under heterogeneous temperature and humidity fluctuation, while reduced initial crossover inhibited formation of harmful radicals ensuring longer lifetime. Despite the negative effects of long-term testing, after 9000 AST cycles NafionPTI(1.5) achieved a maximum power density of 0.468 W cm^{-2} at 90 °C, greater than BoL for Nafion-212 at 80 °C (Figure S4, Supporting Information). High thermal and (electro-)chemical stability, as well as a size that integrates within the Nafion matrix precluding water mediated leaching, preserved PTI-induced performance gain at the end of life (EoL).

2.3. Characterization of Hydrated Environment

To help elucidate the route of improved conductivity and cell performance, WU and swelling ratio (SR) values at 50% and 100% RH were obtained and plotted against PTI wt% in **Figure 3**a,b, respectively (Table S1, Supporting Information). NafionPTI composites exhibited greater WU than RN at both RHs due to the increased presence of hydrophilic groups, enhancing thermodynamic favorability of water retention. Uptake and retention of water molecules (≈9 wt%) residing within the $C_{12}N_{12}H_3$ voids of PTI may also retain water as a reservoir down to low RH.[24] At 100% RH, above the percolation threshold, WU and SR increased from 0 to 1 wt% PTI, and while SR continued to increase, WU decreased for PTI addition >1 wt%. Increased SR for lower WU above 1 wt% PTI suggests that ionomer domain expansion cannot be accommodated by contraction of the amorphous region causing macroscale swelling of the membrane. It can be inferred that PTI-induced morphological alteration results in free volume increase in the amorphous regions up to 1 wt% PTI, but decreases above 1 wt%. Although water content and nanoscale swelling of Nafion ionic domains permit rapid proton transport via strongly hydrogen bonded water clusters,[36,37] nanoscale morphology and chemical interactions clearly have greater effect on proton transport within the ionic domain.[38] Decreased WU with improved conductivity for NafionPTI(1.5) suggests that a different proportion of occupied hydrated environments exist with free, bound, and semibound environments contributing differently to proton dynamics. At 50% RH, water exists bound (and semibound) in clusters within the polymer

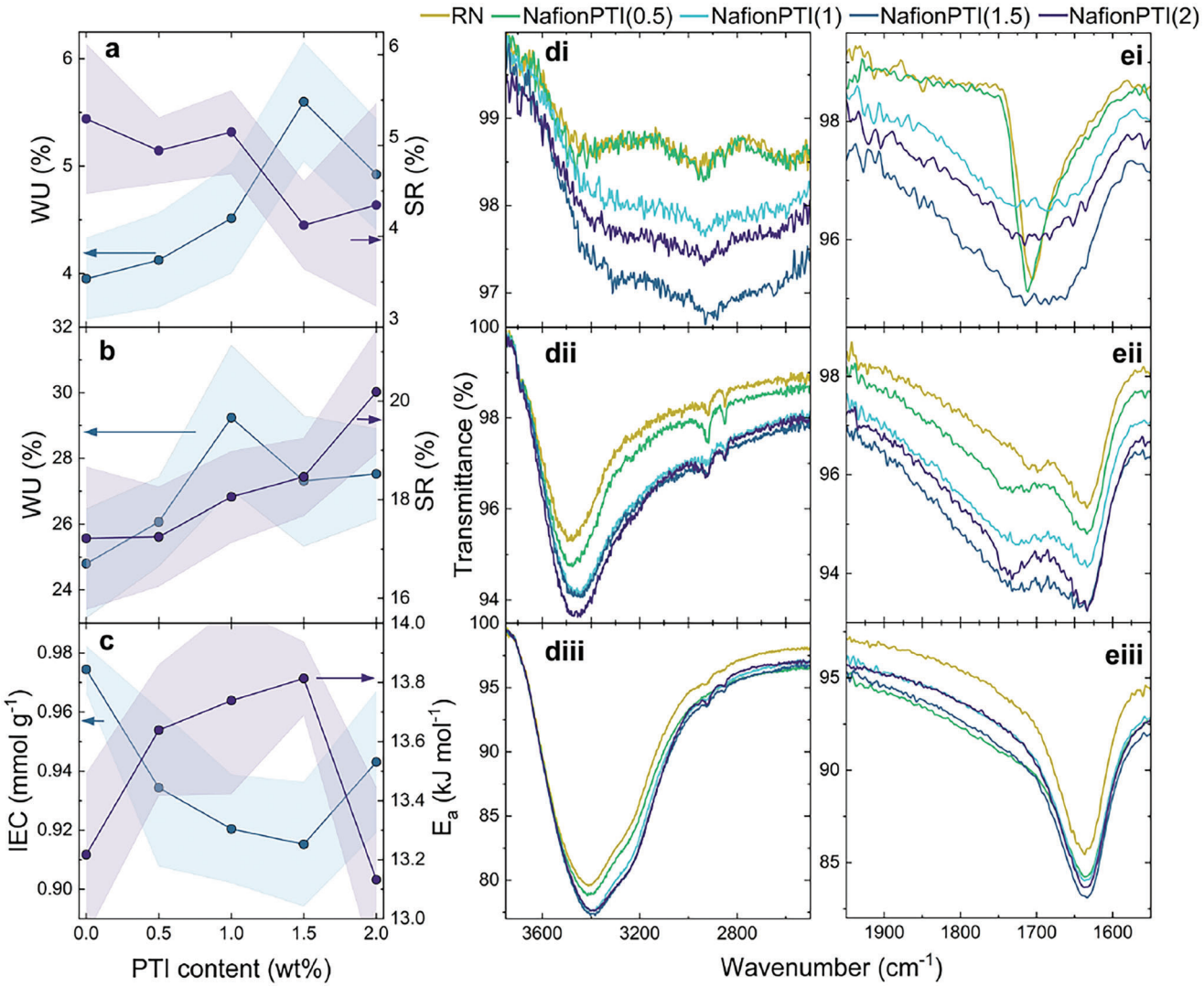

Figure 3. PEM RH-dependent characterization. WU and SR versus PTI wt% at a) 50% RH and b) 100% RH, with the shaded area representing the standard deviation from triplicate measurements. c) IEC and activation energy versus PTI wt%, with the shaded areas representing the standard deviation from triplicate measurements of IEC and error of line fit for E_a. ATR-FTIR spectra highlighting d) ν(OH) and e) δ(HOH) at i) 0% RH, ii) 50% RH, and iii) 100% RH.

matrix rather than forming long-range hydrated networks (i.e. it is below the percolation threshold). A similar WU trend increasing with PTI content was observed but with a peak at 1.5 wt% PTI, suggesting that NafionPTI(1.5) has the most extensive hydrogen bonding network around the hydrated hydronium ion, contributing to greater proton conductivity from low to high RH. Reduced gas crossover can thus be attributed to a twofold change in both polymer chain arrangement, reducing free volume and therefore through-polymer permeation, and increased bound water and electrostatic interactions with PTI reducing water-solvated diffusion of gases. At 50% RH, SR generally reduced with PTI content, in contrast to the WU. PTI may function as molecular scaffolding, restricting collapse of ionic domains, and encouraging greater WU at low RH, and reducing the swelling/restructuring required to accommodate water when below the percolation threshold.[39]

To further understand the influence of chemical properties on internal morphology and additive interactions, ion exchange capacity (IEC) was determined via the titration technique, providing a measure of accessible cation sites. Shown in Figure 3c, IEC reduced with PTI addition, to a minimum of 0.92 mmol g^{-1} for NafionPTI(1.5). This reduction was expected as more of the membrane mass was composed of nonionic PTI, but may also be a result of coordination of anionic groups with PTI functional groups leading to fewer cation exchange sites being available in the modified composite morphology.[40] The structural void of PTI contains three N–H bridges and six pyridinic nitrogen atoms that are capable of hydrogen bonding interactions.[23,24] For PTI mass loadings of 0.5, 1, 1.5, and 2 wt%, the percentages of PTI voids to SO_3^- sites were calculated to be 2.3, 4.6, 6.9, and 9.2% (Supporting Information). This ratio follows closely with the percentage drop in IEC of 3.5%, 5%, and 6% for 0.5, 1, and

1.5 wt% PTI, respectively, suggesting that IEC loss could be a result of sulfonate groups interacting with PTI. These interactions would most likely act through a protonated crosslink, reducing the quantity of ionic groups capable of forming ionic multiplets, observed as a loss in IEC. These altered interactions can therefore have a substantial effect on ionomer morphology and formation of ionic domains. NafionPTI(2) only had a 3% reduction in IEC, supporting a lack of ionic group interactions with PTI when the matrix threshold was exceeded.

Figure S7 (Supporting Information) shows attenuated total internal reflectance Fourier transform infrared (ATR–FTIR) spectroscopy analysis of PEMs under dry, 50%, and 100% RH equilibration, which allowed polymer, ion, and water environments to be elucidated. $\nu_s(CF_2)$ values from the backbone and side chain units that exist in a variety of orientations within the multifarious semicrystalline polymer structure result in broadbands at 1200 and 1150 cm^{-1}. Figure S8a,b (Supporting Information) shows both $\nu_s(CF_2)$ and $\omega(CF_2)$ at 626 cm^{-1} related to the crystalline phase of polytetrafluoroethylene (PTFE), to undergo an increasing redshift with greater PTI addition, confirming interference and modification of the polymer packing. ν(CS) appears as a shoulder to $\omega(CF_2)$ at 636 cm^{-1}, to which PTI caused a redshift in hydrated samples (Figure S8c, Supporting Information). ν_s(COC) at 970 cm^{-1} for the side chain ether that connects the sulfonate group had a redshift and intensity growth with PTI addition (Figure S8e, Supporting Information).[41] Above the Nafion glass transition, greater long-range mobility and dynamic freedom result in a similar peak shift, suggesting that PTI may interrupt the electrostatic forces that constrain molecular dynamics, allowing more stable ion multiplets and larger ionic domains to form.[42,43] The redshift and narrowing of $\nu_s(SO_3^-)$ at 1060 cm^{-1} with RH increase, shown in Figure S8d (Supporting Information), are assigned to ion pair dissociation from SO_3^-–H^+–H_2O to SO_3^-–$H_3O^+(H_2O)_{\lambda-1}$, as the hydration shell grows. The redshift observed in Figure S8d,e (Supporting Information) of NafionPTI composites at 0% RH was thus evidence that PTI stabilized greater dissociation of the ion pair. In addition, the H_3O^+ stretching band at 2920 cm^{-1} (Figure 3d), present at all RH, increased in intensity and redshifted as PTI content increased to 1.5% at 0% RH. This stronger hydrogen bonding is further evidence of ion dissociation forming a stabilized proton complex available for proton dynamics and a stabilized route for low RH conduction, i.e., acid–base pairing.[44]

NafionPTI composites retained a greater quantity of strongly hydrogen bonded water at all hydration states, observed from a greater intensity and redshift of the broad ν(OH) peak at ≈3400 cm^{-1} in Figure 3d.[41,45] This difference became more prominent as the RH decreased, confirming the ability of PTI to retain greater water contents at low RH. In dry RN, a sharp asymmetric bending δ(HOH) peak was observed at 1705 cm^{-1}, associated with H_3O^+ formed upon ion pair dissociation utilizing the residual water molecule at $\lambda = 1$ (Figure 3e).[41] At 50% RH, this peak remained due to the existence of additional protonated complexes such as $H_5O_2^+$/$H_9O_4^+$, but was obscured by a growing δ(HOH) band at 1632 cm^{-1}, assigned to vibrations of water molecules with weak hydrogen bonding in the continuous hydrated phase that permits long-range proton transport formed above the percolation threshold. At 100% RH, only the peak at 1632 cm^{-1} is clearly visible, with asymmetric broadening to higher wavenumbers highlighting the remaining existence of protonated complexes. At 0% RH, NafionPTI(0.5) had a slight blueshift of the H_3O^+ peak due to stronger hydrogen bonding. However, a significant change occurred for 1–2 wt% PTI with a broad peak observed up to 2000 cm^{-1}. Increasing intensity and wavenumber with PTI content suggest that the protonated complexes form with a distribution of stronger hydrogen bonds due to the presence of additional hydrogen bond acceptors and donors that stabilize the protonated water.[34,46] While no definitive peak was observed at 1632 cm^{-1}, as PTI content increased to 1.5 wt% a growing shoulder was observed in this region as PTI induces formation of a hydrogen bonding network at low RH. This hydrogen bonding network could be due to a region of bound water interacting with PTI nitrogen groups or water molecules intercalated within PTI sheets.

At 50% RH, the asymmetric bending δ(HOH) peak (Figure 3e) increased in intensity and blueshifted from 1710 to 1740 cm^{-1} with greater PTI content, indicating an increasing quantity of stronger hydrogen-bonded proton complexes. At 50% and 100% RH the 1632 cm^{-1} peak grew in intensity and width with PTI content to a maximum for 1.5 and 2 wt%. According to Leuchs and Zundel,[47] a greater absorbance at 1632 cm^{-1} occurs for a greater internuclear O–O distance in the proton complex as a result of strong complex binding with the environment. The greater absorbance of the δ(HOH) peak alongside a blueshift in the asymmetric bending δ(HOH) peak suggests PTI affects the hydrogen bonding of the proton complex facilitating longer range proton transfer mechanism analogous to hydrated acid–base pairs. We can conclude that with PTI inclusion increased quantity of water and degree of hydrogen bonding within the hydrated network at given RHs, provide more stable ionic clusters as well as a less rigid humidity-dependent transition between localized and long-range transport.[48]

Activation energy of proton conduction (E_a), derived from Figure S6 (Supporting Information) and plotted in Figure 3c, increased from 13.2 ± 0.3 to 13.8 ± 0.1 kJ mol^{-1} from 0 to 1.5% PTI. Values slightly greater than the energy needed to break a hydrogen bond in bulk water ≈8 kJ mol^{-1} match with previous studies that support a Grotthuss-dominated mechanism.[49,50] The jump in E_a for NafionPTI(0.5–1.5), which increased slightly with PTI content, may be a result of proton transport though the modified hydrated environment of bound/semibound water with stronger hydrogen bonds and acid–base interactions. A return to an E_a of 13.13 ± 0.3 kJ mol^{-1} in NafionPTI(2) suggests the additional E_a in NafionPTI(0.5–1.5) is not due to a separate process occurring solely within PTI and instead the Nafion–PTI interaction is key for the altered mechanism, by creating a new water environment with modified interactions and thus dynamics.[1] Proportionate E_a increase with stronger complex binding observed from FTIR with a PTI content up to 1.5% suggests greater PTI quantity induced more of the modified hydrated environment.

2.4. Composite Morphology

PEM surfaces were measured with tapping mode AFM to understand differences in phase separation due to PTI incorporation. Topography images, shown in Figure S9 (Supporting Information), showed little noticeable difference between films

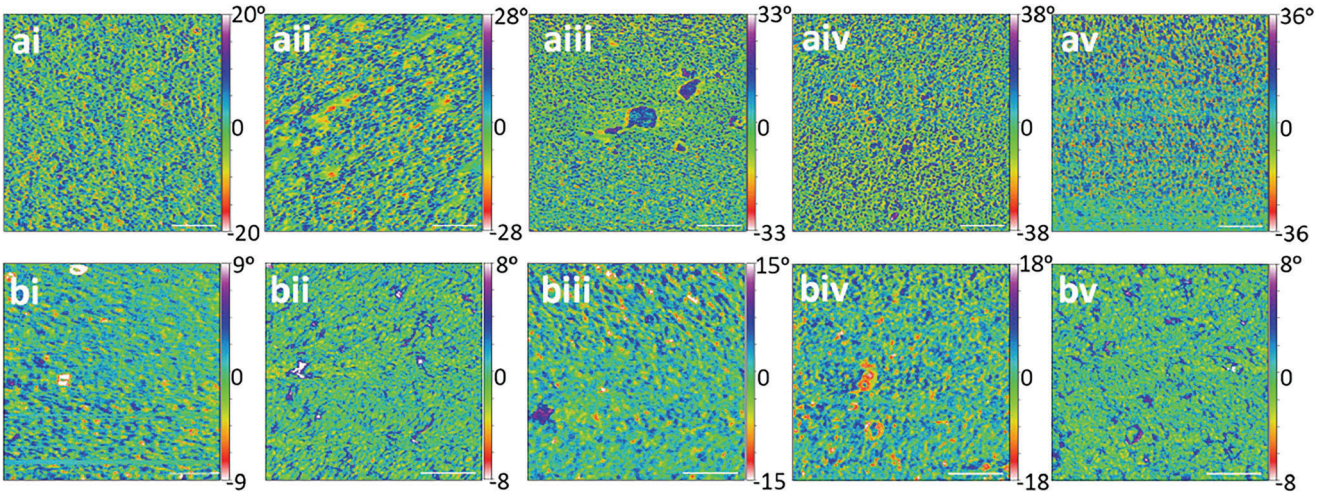

Figure 4. AFM phase images of Nafion films at a) 0% RH and b) 50% RH with PTI contents i) 0 wt%, ii) 0.5 wt%, iii) 1 wt%, iv) 1.5 wt%, and v) 2 wt%; scale bars = 100 nm.

due to the nanoscale size of PTI filler. However, phase imaging of the surface of dry and ambient films in **Figure 4**a,b, revealed differences in viscoelasticity which can be extended to understanding of molecular arrangement in the bulk. Soft ionic phase domains caused negative phase angle change, appearing as green/yellow/red areas, while hard hydrophobic phases caused positive angle change appearing as blue/purple areas.[51] The observed surface structure of randomly orientated hard polymeric aggregates surrounded with soft hydrophilic ionic groups matches well with the model proposed by Gebel and Diat.[52] For 0–1.5 wt% PTI, increased PTI incorporation resulted in increased phase angle difference between the hydrophilic and hydrophobic domains and RMS roughness increased from 5.8° to 13° and from 2.8° to 6.0° for RN to NafionPTI(1.5) in the dry and hydrated states, respectively. This stronger phase separation matches FTIR analysis that indicates stronger hydrogen bonding providing a well-defined ionic pathway in the ionic domains. In contrast, NafionPTI(2) exhibited a reduction in phase separation suggesting excessive PTI caused detrimental phase mixing. From 0 to 50% RH, a larger proportion of the surface was found to be soft, and ionic domains could be seen to visibly swell suggesting polymer restructuring upon WU.

At 50% RH, NafionPTI(0.5 and 2) surfaces appeared to be formed of clusters of hydrophilic domains contained within an intermediate phase, highlighted in Figure S10 (Supporting Information). Based on the size of these features (50–100 nm), this phase could be inferred as visualization of the secondary aggregates.[14,15,52,53] On closer inspection, these features are less defined, but visible in all samples at 50% RH. Only a few small aggregates were visible in RN, but more prominent larger aggregates formed as PTI content increased from 0 to 1 wt% PTI and plateaued for 1–2 wt%, suggesting that the presence of PTI particles induced aggregate enlargement.[54] Intermediate PTI incorporation, between 1 and 1.5 wt%, showed the greatest conductivityand appeared to increase connectivity of ionic domains in both 0 and 50% RH, observed as narrower polymer fibers in a homogeneous soft conductive matrix. NafionPTI(1 and 1.5) also showed regions of increasingly negative phase shift that formed in a "stretched" geometry compared to those observed in RN. This could be due to domains branching together with increasing interconnectivity or could be evidence of PTI conferring 2D character to polymer regions.

While AFM provides direct nanoscale information of surface morphology, it cannot be definitively correlated to internal structures. Small-angle X-ray scattering (SAXS), however, provides information on bulk morphology from size and shape of nanoscale correlations, with Nafion possessing several regions of interest, as seen in **Figure 5**a. Due to their relatively large lateral dimension (30–140 nm), PTI flakes were expected to organize in the bulk matrix, where such long-range structures become resolvable at low angles. As seen in Figure 5a-ii, dry samples show a clear deviation in slope observed in the low angle region. The small Q upturn of RN characterized by a power law $I(Q) \sim Q^{-4}$ was indicative of sharp interfaces within the phase-separated morphology. However, the exponent decreased as greater PTI quantities were incorporated, resulting in a power law of Q^{-2} for NafionPTI(1.5), associated with increasing 2D nature in the morphology such as disk-like or lamellae morphology.[55] This deviation from 3D morphology suggests that polymer aggregates undergo large-scale alignment with the rigid, flat PTI flakes. With further PTI increase, NafionPTI(2) exhibited a slope of Q^{-3} and therefore less 2D nature, evidence that this low angle deviation was not just due to direct observation of PTI sheet structure, but the effect of PTI presence on Nafion. This interaction and alignment with PTI molecular scaffolding induce less tortuous long-range transport networks and greater aggregate rigidity mitigating conductivity losses due to restructuring below the percolation threshold. The greater SR observed for NafionPTI(1.5) and NafionPTI(2) at 100% RH was likely a result of alignment-induced affine expansion with domain water uptake.[39] In comparison for ≤1 wt% PTI, less aggregate "alignment" resulted in greater free volume that concealed WU-induced expansion into randomly distributed polymer fibrils.

The semicrystalline morphology of Nafion was revealed in the scattering spectra (Figure 5a) with an amorphous peak at 1.1 $Å^{-1}$ and a superimposed crystalline peak prominent on the

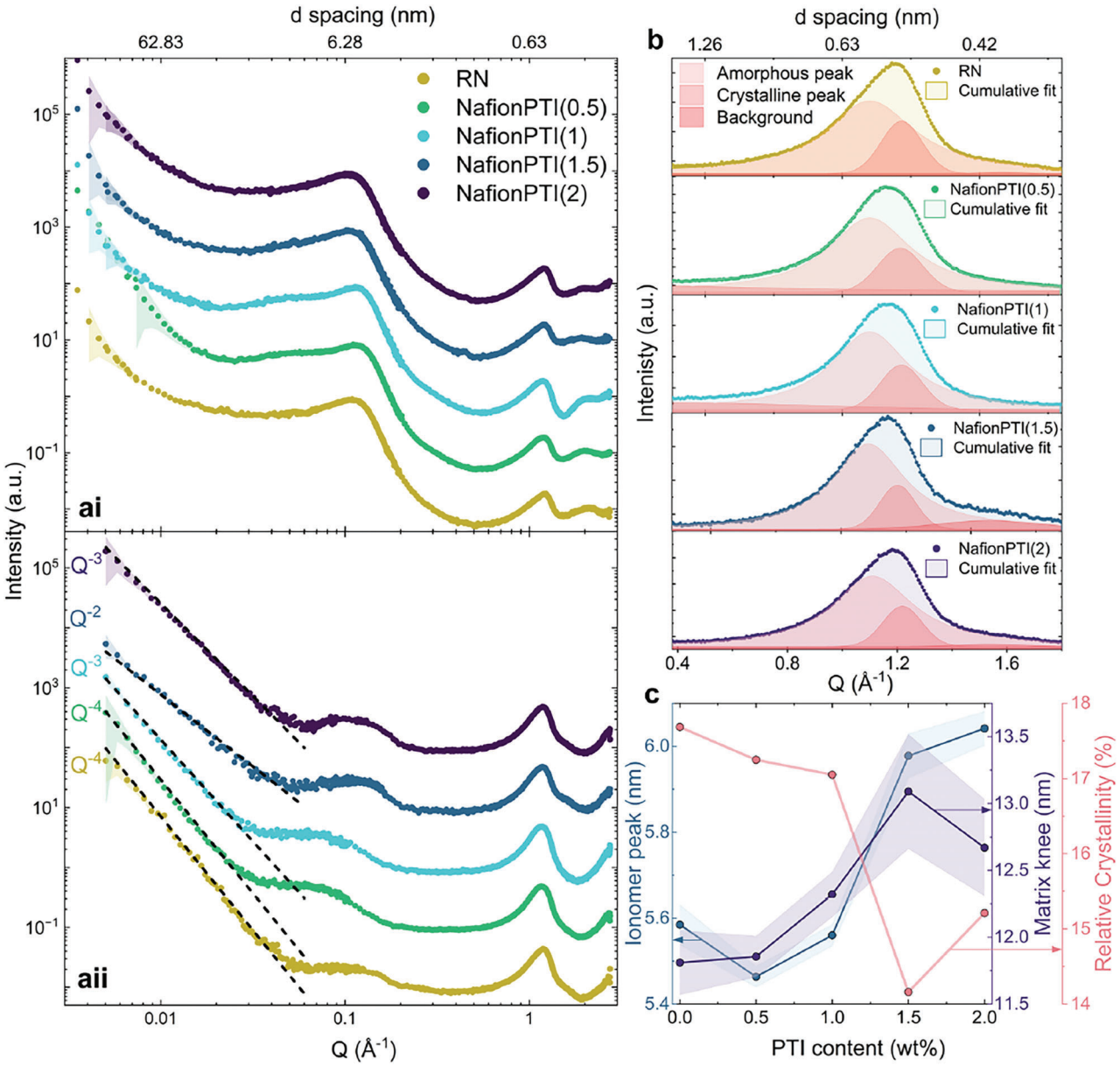

Figure 5. X-ray scattering characterization. a) Double logarithmic small- and wide-angle X-ray scattering of PEMs under i) 100% RH and ii) 0% RH. b) Deconvolution of amorphous and crystalline components of the peak at 1.1–1.24 Å^{-1}. c) Obtained ionomer domain size, matrix knee, and relative crystallinity plotted versus PTI wt% with the shaded area representing the error in peak deconvolution.

right shoulder at 1.24 Å^{-1}. A "matrix knee," at ≈0.05 Å^{-1}, was due to intercrystallite spacing separated by amorphous and ionic regions of polymer, with a correlation length of ≈12 nm.[57] Deconvoluting the peak at 1.1 Å^{-1}, shown in Figure 5b, provided the relative degree of crystallinity, and deconvolution of the low Q region in Figure S11 (Supporting Information) provided the matrix knee. These parameters are shown to be inversely proportional in Figure 5c, with intercrystallite correlation growing with greater PTI content from 11.8 nm to a peak of 13.1 nm in NafionPTI(1.5), before a slight decrease to 12.7 nm for NafionPTI(2), while relative crystallinity decreased from 17.7% to a minimum of 14.2% for NafionPTI(1.5) before a slight increase to 15.2% for NafionPTI(2). Nafion crystallites are formed from side-chain-deficient CF_2 groups, and low crystallinity is associated with disruption induced by side chains. The matrix knee shift and reduced prominence with PTI wt% are evidence that PTI disrupts the matrix packing, increasing the spacing between Nafion crystallites. Reduced crystallinity indicates that PTI altered the arrangement of ion-deficient chain segments so that fewer contribute to crystallite growth. More chains are therefore available in the amorphous region creating greater free volume and providing more degrees of freedom for ionic side chains to assemble into larger ionic domains, supported by the shift in ν_s(COC).[57]

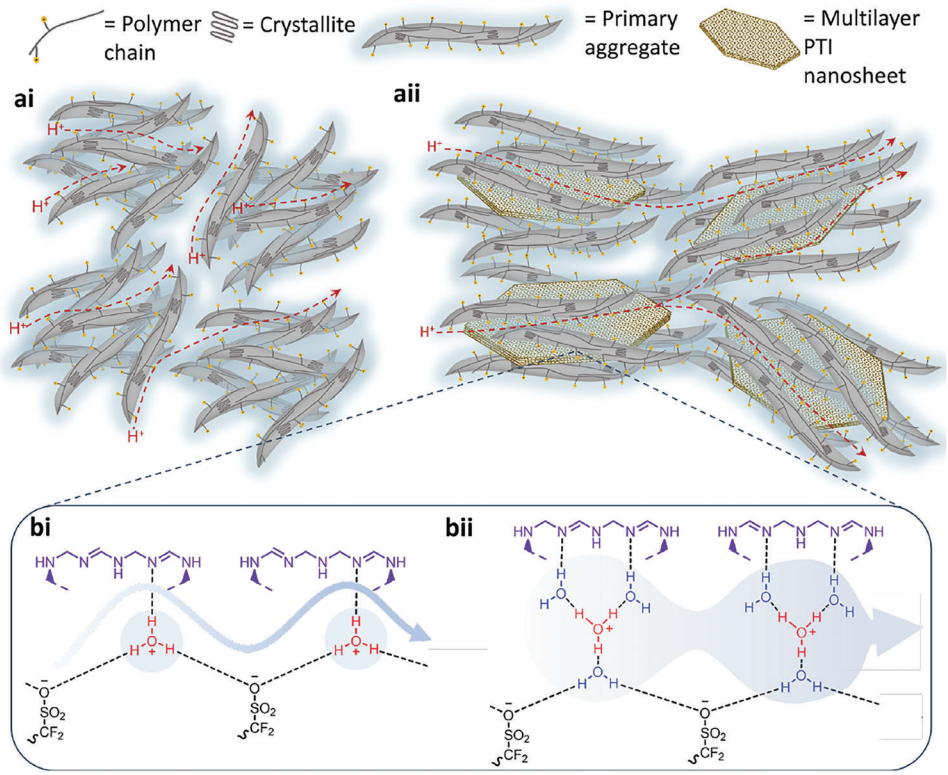

Figure 6. Schematic of PTI matrix tuning and acid–base interactions. a-i) Accepted large-scale structure of pure Nafion with ribbon-like primary aggregates that form secondary aggregate "bundles" and nanophase separate to provide ionic domains that connect across aggregates to provide long-range transport. a-ii) Structural tuning of Nafion due to PTI resulting in larger aligned secondary aggregate-PTI clusters, and smaller and further spaced crystallites that collectively result in improved long-range transport within and between secondary aggregates. b) Schematic of facilitated proton transport via acid–base interactions between Nafion sulfonate and PTI pyridinic nitrogen lone pairs with i) dissociated hydronium bridge stabilized in dry conditions and ii) stabilized Eigen ions at low humidity.

The ionomer peak, corresponding to structural correlation of ionic domains, appears at slightly lower Q for these PEMs in Figure 5a-i, due to larger domains formed when casting with the larger Na^+ cation.[58] Ionomer peak deconvolution is shown in Figure S11 (Supporting Information), and ionomer domain change with PTI content is shown in Figure 5c. Domain size decreased for 0.5 wt% PTI, but greater PTI wt% resulted in ionic domain expansion up to a maximum for 2 wt%, corresponding with greater macroscale SR. Larger ionic domains provide larger hydrogen-bonded networks with greater coordination, for faster proton hopping in confined voids.[45,59] As WU of the composites increased to a maximum for 1 wt%, domain size cannot solely be a result of water volume and instead due to polymer–PTI interactions. The inverse relationship of ionomer peak and crystallinity in Figure 5c evidenced the interrelation of these two polymer features. Increased amorphous polymer with increased side chain freedom and FTIR shifts of the side chain resulted in stabilization of larger ionic clusters. The larger separation of smaller crystallites in NafionPTI(0.5) agrees with the morphology from AFM with evenly distributed but smaller hydrophilic regions. The increases in WU and SR for NafionPTI(0.5) and NafionPTI(1) suggest the existence of more, connected but narrower ionic domains leading to intermediate conductivity enhancements.

3. Discussion

The above characterization demonstrates that PTI has two synergistic interactions with Nafion, namely polymer matrix tuning and altering the hydrated ion environment, as depicted in **Figure 6**. SAXS found that the polymer aggregates align with the large flat PTI sheets, and WU/SR measurements suggested PTI addition up to 1 wt% increased free volume, before decreasing for 1.5 and 2 wt%. This trend follows the sharp transition in ionomer domain size and crystallinity between 1 and 1.5 wt% where a larger amorphous proportion in NafionPTI(1.5) stabilizes densely ordered polymer packing and larger ionic domains. This aligned morphology with the PTI molecular scaffolding provides a greater proportion of connected networks that are retained at low and intermediate RH and swell with WU, minimizing charge polarization across the nonionic domains and increasing the mean free path for proton transport, as previously observed in artificially oriented Nafion.[57] Sulfonate anchoring interactions with N–H groups in PTI provide nucleation sites that stabilize primary aggregate alignment, forming clusters around the sheets, and induce the growth of secondary aggregates.[54,60] Increased aggregate size reduces the proportion of interaggregate space, decreasing tortuosity and long-range resistance.[61] The resulting network with increased ordering, larger ionic domains,

and fewer "dead-end" channels resultes in long-range dynamic connections, facilitating efficient proton and water transport.

PTI hydrophilic structural voids induce significant increases to WU with an increasing quantity of PTI forming greater proportions of structured water. A greater E_a in this hydrated environment supplements proton conduction at low and high RH. FTIR peaks at 2900, 1740–1630, and 1060 cm^{-1} support the theory of acid–base interactions between the pyridinic/triazine nitrogen and hydrated sulfonic acid.[46] Heterogeneously distributed regions of the polymer, exhibiting a SO_3–H_3O^+–PTI interface, provide a facilitated proton transfer mechanism, as shown in Figure 6b.[19] The surface mechanism is enabled by the additional acid–base transfers which destabilize the strong sulfonate–hydronium bond.At low RH, nitrogen-baseinduced dissociation of the sulfonic acid undergoes ultrafast proton transfer to form an encounter pair with greater hydronium coordination, analogous to that of an Eigen ion ($H_9O_4^+$).[44] With increased WU, water-bridged proton complexes form, such as Eigen complexes, and are stabilized in comparison to existence in bulk water. A hydrogen-bonded water wire of hydrated complexes channels protons efficiently in a rapid Grotthuss type proton conduction in the hydrated state.[44,48] A declining performance from exceeding the threshold limit of 1.5 wt% PTI is shown to be a result of many large sheets interrupting large-scale polymer morphology and increasing relative crystallinity, while reducing intercrystallite separation and connectivity of hydrophilic regions for long-range proton transport.

4. Conclusion

In this work, composite proton exchange membranes with significantly enhanced proton conductivity and water management were manufactured through scalable USP deposition and demonstrated for PEMFC applications. It was shown that the incorporation of PTI, a functional hygroscopic additive, simultaneously directed long-range connectivity of polymer aggregate clusters, and coordinated acid–base interactions to facilitate both long-range transport and stabilized proton dynamics at low and high RH, mitigating the effect of cell hydration heterogeneities. Hence, it was demonstrated that when appropriate materials are utilized, low-percentage multifunctional nanomaterial additives can effectively influence the behavior of polymeric membranes.

Incorporation of PTI, with an appropriate size of 30–140 nm, into the PFSA host matrix increased proton conductivity by over 50% at 100% RH and over 140% at 20% RH, when compared to a pure Nafion membrane prepared in the same way. This performance enhancement was sustained when the composite PEMs were used in operating fuel cells, achieving a maximum power density of 0.714 W cm^{-2}, compared to 0.462 W cm^{-2} for commercially manufactured Nafion-212, and 85% greater current density at 0.6 V. To the best of the authors' knowledge, this is the greatest reported power and current increase to an H_2/air fuel cell enabled by the use of a bulk composite membrane based on Nafion, showing huge potential of PTI to provide required device efficiencies for a relatively facile and cheap material addition.[62,63] This composite therefore both sets a new benchmark for PEM performance and, more widely, offers a route toward the tuning of numerous functional polymer systems, across membranes and beyond.

5. Experimental Section

Synthesis of PTI and Preparation of Exfoliated Solution: The starting PTI·LiCl crystals used in this study were obtained by polymerization of dicyandiamide ($C_2N_4H_4$) in a LiCl/KCl eutectic molten salt mixture in an evacuated fused silica tube at 600 °C. After synthesis, excess salt was removed by washing in water and ethanol. The resulting intercalated crystalline solids have a composition of $C_{12}N_{17.5}H_{6.3}Cl_{1.5}Li_{3.2}$ (by use of X-ray photoelectron spectroscopy (XPS), bulk analysis, and solid-state ^{7}Li NMR); the crystallinity was characterized using total X-ray powder scattering with pair distribution function (PDF) analysis.[64] The intercalated Li^+ and halide ions were removed by continuously washing the samples in H_2O via Sohxlet extraction over 21 days. The result was a fully deintercalated crystalline PTI material (IF-PTI) with a layered structure and composition of $C_6N_9H_3$.[29] IF-PTI powder was ground in pestle and mortar for 20 min followed by dispersion in DMF (Fischer Chemical, 99.8%) for 1 week, allowing unexfoliated PTI to sediment and the exfoliated PTI/DMF (0.1 mg mL^{-1}) dispersion to be extracted from the top.

Preparation of NafionPTI Composite: Nafion 212 (1 g) was added to 100 mL water:ethanol mixture (50:50 v/v) and heated to 240 °C in a sealed high-temperature vessel at ≈40 bar for 24 h. After cooling, a clear, homogeneous, colorless alcohol-free PFSA dispersion was prepared by continuous azeotropic distillation at 70 °C for 24 h. The dispersion was then neutralized with drop wise addition of NaOH (0.1 M) and dried at 60 °C until a brittle transparent film formed. Finally, the formed PFSA crystals were ground into a fine white powder. The recast PFSA crystals were then dissolved in a volume of DMF or PTI/DMF to achieve desired PTI wt%. The dispersion was then sonicated for 15 min, to ensure full dissolution and dispersion of Nafion and PTI, followed by stirring for 24 h.[32] The Nafion/PTI/DMF solutions were then ultrasonic spray-printed onto a flat glass substrate at 140 °C with a flow rate of 0.25 mL min^{-1} to produce a 50 µm film. The cast polymers were then dried and annealed in a vacuum oven at 80 °C for 12 h and 160 °C for 2 h, respectively. Composite films were then soaked in water before peeling off the substrate and immersing in the following order to each solution for 1 h; H_2O_2 (3 wt%), DI water, H_2SO_4 (1 M) at 80 °C and finally stored in water until use.

Characterization: The PTI solution was dropcast onto a mica substrate and dried under vacuum to remove solvent, before AFM imaging. AFM images of films held with carbon tape were produced by operating a Bruker Dimension Icon AFM in tapping mode with an SNL-A probe (nominal tip radius = 2 nm; resonance frequency = 65 kHz; and spring constant = 0.35 N m^{-1}) with a scan rate of 0.5 Hz and 512 scans per line. 0% RH measurements were carried out in an argon-filled glove box (LABStar, MBraun) while 50% RH measurements were obtained in ambient air. A single cantilever maintained at the same drive amplitude and set point throughout the measurements was used for the sample matrix. FTIR spectra were recorded on a Bruker Alpha Fourier transform infrared spectroscopy instrument between 400 and 4000 cm^{-1} for 64 averaged scans at 1 cm^{-1} resolution with autosubtracted background. RH control of samples was achieved using the same procedure as detailed in water uptake and swelling ratio experimental.

Ion Exchange Capacity (Acid–Base Titration): About 100 mg of the sample was soaked in NaCl (2 M, 50 mL) for 24 h to exchange H^+ with Na^+ ions. The displaced H^+ ions were measured by titrating the resulting solution (NaCl/HCl) against NaOH (0.01 M) using an autotitrator (Metrohm 848, TitrinoPlus) with pH probe. Three samples, each separately prepared from different PFSA precursor and PTI/DMF solutions, were measured and IEC of each calculated using the following equation

$$\mathrm{IEC}\left(\mathrm{mmol\ g^{-1}}\right) = \frac{V_{\mathrm{NaOH}} \times C_{\mathrm{NaOH}}}{M_{\mathrm{dry}}} \quad (1)$$

Water Uptake and Swelling Ratio: Three membrane samples of ≈9 cm^2, each separately prepared from different PFSA precursor and PTI/DMF solutions, were immersed in DI water at 25 °C for 24 h. After that membranes were carefully blotted of all residual surface water and the fully hydrated membrane sample was rapidly weighed and thickness measured using a micrometer gauge. The membrane samples were then

equilibrated at 50% RH ($Mg(NO_3)_2$ saturated salt solution) for 24 h before repeating measurements. Finally, samples were dried for 24 h at 80 °C under dynamic vacuum in a Buchi tube and measurements performed in an argon-filled glove box (LABStar, MBraun) with H_2O and O_2 levels being kept below 0.5 ppm to obtain the dry values. Three specimens were tested for each sample. WU and SR were obtained with Equations (2) and (3)

$$\mathrm{WU} = \frac{W_{\mathrm{hyd}} - W_{\mathrm{dry}}}{W_{\mathrm{dry}}} \times 100\% \tag{2}$$

$$\mathrm{SR} = \frac{T_{\mathrm{hyd}} - T_{\mathrm{dry}}}{T_{\mathrm{dry}}} \times 100\% \tag{3}$$

where W_{hyd} and W_{dry} are the masses of hydrated (50 or 100%) and dry membranes, respectively, and T_{hyd} and T_{dry} are the thickness of hydrated (50 or 100%) and dry membranes, respectively.

Proton Conductivity: In-plane proton conductivity of polymer electrolyte membranes was determined using a four-point probe method. Four equally spaced platinum electrodes were held in contact with the membrane, with two used to apply a current through the membrane while the other two measured the voltage drop. Proton conductivity of the membrane at different temperatures and RH was probed by AC impedance spectroscopy using a frequency response analyzer (Gamry, UK) with an oscillating voltage of 10 mV over a frequency range from 1 MHz to 1 Hz. The impedance (resistance) value corresponding to the *x*-intercept of the real axis at the low-frequency region was used to calculate the proton conductivity according to Equation (4)

$$\sigma = \frac{L}{R \times W \times T} \tag{4}$$

where σ is the proton conductivity of the membrane (S cm^{-1}), L = 0.425 cm, is the fixed distance between two Pt electrodes; R is the membrane resistance (Ω); W is the width of the sample (cm), and T is the thickness of the membrane (cm). Average values were obtained by repeating measurements on three samples each separately prepared from different PFSA precursor and PTI/DMF solutions; data with standard deviation are shown in Figure S6 (Supporting Information). The E_a of proton conduction was derived by fitting the data $\ln(\sigma T)$ versus $1000/T$. The temperature-dependent proton conductivity was fulfilled for a semiempirical Arrhenius equation $\sigma = A\exp(\frac{-E_a}{RT})$, where σ is the proton conductivity (S cm^{-1}), A is a pre-exponential factor, E_a is the activation energy of proton migration (kJ mol^{-1}), R is the universal gas constant (8.31 J mol^{-1} K^{-1}), and T is the absolute temperature (K).

SAXS and WAXS Sample Preparation and Analysis: Sample films equilibrated at 0 and 100% RH (and bulk PTI powder) were inserted into 1.5 mm borosilicate glass capillary tubes and hermetically sealed. SAXS/wide-angle X-ray scattering (WAXS) was carried out on a Ganesha 300XL, Xenocs, France. Microfocus X-ray (λ = 1.54 Å) was generated from a copper source with a motorized collimation system of four-blade single crystal slits. Movable solid-state photon-counting detector (PILATUS 300 K, Dectris AG, Switzerland) was mounted on an uninhibited transverse rail along the beamline. The SAXS/WAXS system was calibrated using lanthanum hexaboride and validated on the day of measurement with silver behenate. Ultra–small angle X–ray scattering (USAXS, 0.003–0.2 $Å^{-1}$), SAXS (0.005–0.3 $Å^{-1}$), and WAXS (0.1–2.75 $Å^{-1}$) were acquired with 1200, 600, and 180 s exposure times, respectively, under $<10^{-2}$ mbar vacuum. The scattering intensity as a function of Q was obtained from a radial integration of each scattering image, and scattering from an empty capillary tube was used for background subtractions. Data reduction and processing were performed using Ganesha ICC software. The WAXS peaks at 1.12 $Å^{-1}$ (I_a) and 1.24 $Å^{-1}$ (I_c) of the dry samples were fitted to Lorentzian and Gaussian functions, respectively. The ratio of integrated intensity for the crystalline and total intensity was calculated with the following equation to obtain the effective crystallinity

$$x_c = \frac{\int q^2 I_c(q)\, dq}{\int \left(q^2 I_c(q) + q^2 I_a(q)\right) dq} \tag{5}$$

Fuel Cell Assembly and Testing: After acid pretreatment and washing, the membranes were dried in appropriate frames at room temperature, before being sandwiched between commercially available Hyplat gas diffusion electrodes (0.4 mg_{Pt} cm^{-2}) and hot-pressed at 135 °C and 440 PSI for 3 min to form the MEAs. MEAs with 5 cm^2 active area were assembled in single-cell hardware (Scribner, USA) with a single channel serpentine flow field, using 4.3 N m torque and Teflon gaskets to achieve ≈25% thickness gas diffusion layer (GDL) compression. An 850e fuel cell test station (Scribner Associates, USA) was used to control cell and gas line temperature, gas flow of H_2, and air (0.3 L min^{-1}) feeds at the anode and cathode, respectively. The MEA was activated with constant voltage holds between 0.6 and 0.5 V with retention of these cell voltages until a steady current density was observed. Beginning-of-life PEMFC performance data were collected under controlled galvanostatic discharge steps. The internal Ohmic resistance was estimated using the 850e instrument's internal current interrupt method. The hydrogen crossover was obtained via LSVs at 80 °C with H_2 and N_2 gas flow (0.2 L min^{-1}) at anode and cathode, respectively. LSV was recorded from 0.06 to 0.6 V at a scan rate of 2 mV s^{-1}. Cell cathode was used as the working electrode, and anode was the counter and reference electrodes. The maximum current at 0.4 V was used to quantify the hydrogen crossover of PEM. The "US DRIVE Fuel Cell Technical Team Roadmap" membrane combined chemical/mechanical PEM AST protocol was followed. The cell was operated at 90 °C with cycles of alternating wet (45 s) and dry (30 s) gas streams of H_2/air flow at 0.2 L min^{-1}. Every 1000 cycle's hydrogen crossover was measured.

Supporting Information

Supporting Information is available from the Wiley Online Library or from the author.

Acknowledgements

K.S. and F.F. acknowledge EPSRC for funding (Grant No. EP/V057863/1). A.J.C. would like to thank The Royal Society (University Research Fellowship, URF/R1/221476) for funding. T.S.M. and D.J.L.B. would like to acknowledge support from the EPSRC (Grant Nos. EP/W033321/1, EP/W03395X/1, EP/X023656/1, and EP/P009050/1). D.J.L.B. also acknowledges the Royal Academy of Engineering (Grant No. RCSRF2021/13/53), the National Physical Laboratory (NPL) and HORIBA for supporting his RAEng Research Chair. Finally, the authors would like to thank Dr. Han Wu and the EPSRC CNIE research facility service at University College London for assisting the collection of SAXS/WAXS data.

Conflict of Interest

The authors declare no conflict of interest.

Data Availability Statement

The data that support the findings of this study are available from the corresponding author upon reasonable request.

Keywords

carbon nitride, fuel cells, membrane additives, PEMs, ultrasonic spray printing

Received: April 12, 2023
Revised: May 25, 2023
Published online:

[1] A. Kusoglu, A. Z. Weber, *Chem. Rev.* **2017**, *117*, 987.
[2] M. Maier, K. Smith, J. Dodwell, G. Hinds, P. R. Shearing, D. J. L. Brett, *Int. J. Hydrogen Energy* **2022**, *47*, 30.
[3] R. Tan, A. Wang, R. Malpass-Evans, R. Williams, E. W. Zhao, T. Liu, C. Ye, X. Zhou, B. P. Darwich, Z. Fan, L. Turcani, E. Jackson, L. Chen, S. Y. Chong, T. Li, K. E. Jelfs, A. I. Cooper, N. P. Brandon, C. P. Grey, N. B. McKeown, Q. Song, *Nat. Mater.* **2019**, *19*, 195.
[4] L. M. Aeshala, S. U. Rahman, A. Verma, *Sep. Purif. Technol.* **2012**, *94*, 131.
[5] W. C. F. Grot, G. E. Munn, P. N. Walmsley, presented at *The 141st National Meeting of the Electrochemical Society*, The Electrochemical Society, Houston, TX **1972**.
[6] W. Y. Hsu, T. D. Gierke, *J. Membr. Sci.* **1983**, *13*, 307.
[7] K. I. Winey, R. A. Vaia, *MRS Bull.* **2007**, *32*, 314.
[8] R. R. Abbaraju, N. Dasgupta, A. V. Virkar, *J. Electrochem. Soc.* **2008**, *155*, B1307.
[9] W. F. Chen, J. S. Wu, P. L. Kuo, *Chem. Mater.* **2008**, *20*, 5756.
[10] K.-D. Kreuer, G. Portale, *Adv. Funct. Mater.* **2013**, *23*, 5390.
[11] A. Kusoglu, M. A. Modestino, A. Hexemer, R. A. Segalman, A. Z. Weber, *ACS Macro Lett.* **2012**, *1*, 33.
[12] M. H. Litt, *Polym. Prepr. (Am. Chem. Soc., Div. Polym. Chem.)* **1997**, *38*, 80.
[13] H. G. Haubold, T. Vad, H. Jungbluth, P. Hiller, *Electrochim. Acta* **2001**, *46*, 1559.
[14] L. Rubatat, A. G. Gebel, O. Diat, *Macromolecules* **2004**, *37*, 7772.
[15] L. Rubatat, A. L. Rollet, G. Gebel, O. Diat, *Macromolecules* **2002**, *35*, 4050.
[16] M. Fumagalli, S. Lyonnard, G. Prajapati, Q. Berrod, L. Porcar, A. Guillermo, G. Gebel, *J. Phys. Chem. B* **2015**, *119*, 7068.
[17] R. Kumar, C. Xu, K. Scott, *RSC Adv.* **2012**, *2*, 8777.
[18] B. G. Choi, J. Hong, Y. C. Park, D. H. Jung, W. H. Hong, P. T. Hammond, H. Park, *ACS Nano* **2011**, *5*, 5167.
[19] M. Gang, G. He, Z. Li, K. Cao, Z. Li, Y. Yin, H. Wu, Z. Jiang, *J. Membr. Sci.* **2016**, *507*, 1.
[20] M. R. Karim, K. Hatakeyama, T. Matsui, H. Takehira, T. Taniguchi, M. Koinuma, Y. Matsumoto, T. Akutagawa, T. Nakamura, S.-I. Noro, T. Yamada, H. Kitagawa, S. Hayami, *J. Am. Chem. Soc.* **2013**, *135*, 8097.
[21] W. Wu, Y. Li, J. Liu, J. Wang, Y. He, K. Davey, S.-Z. Qiao, *Adv. Mater.* **2018**, *30*, 1707516.
[22] K. A. Page, W. Jarrett, R. B. Moore, *J. Polym. Sci., Part B: Polym. Phys.* **2007**, *45*, 2177.
[23] D. Burmeister, H. A. Tran, J. Müller, M. Guerrini, C. Cocchi, J. Plaickner, Z. Kochovski, E. J. W. List-Kratochvil, M. J. Bojdys, *Angew. Chem., Int. Ed.* **2022**, *61*, e202111749.
[24] F. Foglia, A. J. Clancy, J. Berry-Gair, K. Lisowska, M. C. Wilding, T. M. Suter, T. S. Miller, K. Smith, F. Demmel, M. Appel, V. G. Sakai, A. Sella, C. A. Howard, M. Tyagi, F. Corà, P. F. McMillan, *Sci. Adv.* **2020**, *6*, eabb6011.
[25] H. Chi, C. Chen, K. Zhao, L. F. Villalobos, P. A. Schouwink, L. Piveteau, K. P. Marshall, Q. Liu, Y. Han, K. V. Agrawal, *Angew. Chem., Int. Ed.* **2022**, *61*, e202207457.
[26] L. Cao, H. Wu, P. Yang, X. He, J. Li, Y. Li, M. Xu, M. Qiu, Z. Jiang, *Adv. Funct. Mater.* **2018**, *28*, 1804944.
[27] S. Liu, X. Zhang, L. Zhang, W. Xie, *Sci. Rep.* **2016**, *6*, 37042.
[28] T. S. Miller, A. B. Jorge, T. M. Suter, A. Sella, F. Corà, P. F. McMillan, *Phys. Chem. Chem. Phys.* **2017**, *19*, 15613.
[29] T. M. Suter, T. S. Miller, J. K. Cockcroft, A. E. Aliev, M. C. Wilding, A. Sella, F. Corà, C. A. Howard, P. F. McMillan, *Chem. Sci.* **2019**, *10*, 2519.
[30] T. S. Miller, T. M. Suter, A. M. Telford, L. Picco, O. D. Payton, F. Russell-Pavier, P. L. Cullen, A. Sella, M. S. P. Shaffer, J. Nelson, V. Tileli, P. F. McMillan, C. A. Howard, *Nano Lett.* **2017**, *17*, 5891.
[31] L. F. Villalobos, M. T. Vahdat, M. Dakhchoune, Z. Nadizadeh, M. Mensi, E. Oveisi, D. Campi, N. Marzari, K. V. Agrawal, *Sci. Adv.* **2020**, *6*, eaay9851.
[32] R. B. Moore, C. R. Martin, *Anal. Chem.* **1986**, *58*, 2569.
[33] M. Klingele, M. Breitwieser, R. Zengerle, S. Thiele, *J. Mater. Chem. A* **2015**, *3*, 11239.
[34] V. Di Noto, M. Piga, S. Lavina, E. Negro, K. Yoshida, R. Ito, T. Furukawa, *Electrochim. Acta* **2010**, *55*, 1431.
[35] R. Borup, J. Meyers, B. Pivovar, Y. S. Kim, R. Mukundan, N. Garland, D. Myers, M. Wilson, F. Garzon, D. Wood, P. Zelenay, K. More, K. Stroh, T. Zawodzinski, J. Boncella, J. E. McGrath, M. Inaba, K. Miyatake, M. Hori, K. Ota, Z. Ogumi, S. Miyata, A. Nishikata, Z. Siroma, Y. Uchimoto, K. Yasuda, K. I. Kimijima, N. Iwashita, *Chem. Rev.* **2007**, *107*, 3904.
[36] D. Hankins, J. W. Moskowitz, F. H. Stillinger, *J. Chem. Phys.* **1970**, *53*, 4544.
[37] S. Akbari, M. T. H. Mosavian, F. Moosavi, A. Ahmadpour, *Phys. Chem. Chem. Phys.* **2019**, *21*, 25080.
[38] V. Sproll, G. Nagy, U. Gasser, J. P. Embs, M. Obiols-Rabasa, T. J. Schmidt, L. Gubler, S. Balog, *Macromolecules* **2016**, *49*, 4253.
[39] M. Rodgers, Y. Yang, S. Holdcroft, *Eur. Polym. J.* **2006**, *42*, 1075.
[40] K. Karan, *Langmuir* **2019**, *35*, 13489.
[41] M. Laporta, M. Pegoraro, L. Zanderighi, *Phys. Chem. Chem. Phys.* **1999**, *1*, 4619.
[42] V. O. Kollath, K. Karan, *Phys. Chem. Chem. Phys.* **2016**, *18*, 26144.
[43] A. Barnett, J. Lu, V. Molinero, *J. Phys. Chem. C* **2021**, *125*, 27703.
[44] O. F. Mohammed, D. Pines, J. Dreyer, E. Pines, E. T. J. Nibbering, *Science* **2005**, *310*, 83.
[45] A. W. Knight, N. G. Kalugin, E. Coker, A. G. Ilgen, *Sci. Rep.* **2019**, *9*, 8246.
[46] M. Falk, *Can. J. Chem.* **1980**, *58*, 1495.
[47] M. Leuchs, G. Zundel, *J. Chem. Soc., Faraday Trans. 2* **1978**, *2*, 2256.
[48] F. Hu, W. Luo, M. Hong, *Science* **2010**, *330*, 505.
[49] L. Liu, W. Chen, Y. Li, *J. Membr. Sci.* **2016**, *504*, 1.
[50] D. E. Hare, C. M. Sorensen, *J. Chem. Phys.* **1990**, *93*, 2669.
[51] R. S. McLean, M. Doyle, B. B. Sauer, *Macromolecules* **2000**, *33*, 6541.
[52] G. Gebel, O. Diat, *Fuel Cells* **2005**, *5*, 261.
[53] A. L. Rollet, O. Diat, G. Gebel, *J. Phys. Chem. B* **2002**, *106*, 3033.
[54] F. Yang, L. Xin, A. Uzunoglu, Y. Qiu, L. Stanciu, J. Ilavsky, W. Li, J. Xie, *ACS Appl. Mater. Interfaces* **2017**, *9*, 6530.
[55] L. A. Feigin, D. I. Svergun, in *Structure Analysis by Small-Angle X-Ray and Neutron Scattering* (Ed: G. W. Taylor), Springer, New York, NY **1987**.
[56] Y. Zhao, K. Yoshimura, T. Motegi, A. Hiroki, A. Radulescu, Y. Maekawa, *Macromolecules* **2021**, *54*, 4128.
[57] J. S. Da Silva, S. G. M. Carvalho, R. P. Da Silva, A. C. Tavares, U. Schade, L. Puskar, F. C. Fonseca, B. R. Matos, *Phys. Chem. Chem. Phys.* **2020**, *22*, 13764.
[58] H. D. Nguyen, T. K. L. Nguyen, E. Planes, J. Jestin, L. Porcar, S. Lyonnard, C. Iojoiu, *J. Phys. Chem. C* **2020**, *124*, 13071.
[59] O. O. Sofronov, H. J. Bakker, *ACS Cent. Sci.* **2020**, *6*, 1150.
[60] S. Ott, A. Orfanidi, H. Schmies, B. Anke, H. N. Nong, J. Hübner, U. Gernert, M. Gliech, M. Lerch, P. Strasser, *Nat. Mater.* **2020**, *19*, 77.
[61] S. Lyonnard, *Adv. Struct. Mater.* **2013**, *34*, 163.
[62] Y. Kim, K. Ketpang, S. Jaritphun, J. S. Park, S. Shanmugam, *J. Mater. Chem. A* **2015**, *3*, 8148.
[63] Q. Zhang, S. Dong, P. Shao, Y. Zhu, Z. Mu, D. Sheng, T. Zhang, X. Jiang, R. Shao, Z. Ren, J. Xie, X. Feng, B. Wang, *Science* **2022**, *378*, 181.
[64] M. J. Bojdys, J. O. Müller, M. Antonietti, A. Thomas, *Chem.- Eur. J.* **2008**, *14*, 8177.